Numerical investigation of the propagation of shock waves in rigid porous materials: development of the computer code and comparison with experimental results

By A. LEVY[1], G. BEN-DOR[1] AND S. SOREK[2]

[1] Pearlstone Center for Aeronautical Engineering Studies, Department of Mechanical Engineering, Ben-Gurion University of the Negev, Beer Sheva, Israel

[2] Water Resource Research Center, J. Blaustein Desert Research Institute, Ben-Gurion University of the Negev, Sede Boker Campus, Israel

The governing equations of the flow field which is obtained when a thermoelastic rigid porous medium is struck head-one by a shock wave are developed using the multi-phase approach. The one-dimensional version of these equations is solved numerically using a TVD-based numerical code. The numerical predictions are compared to experimental results and good to excellent agreements are obtained for different porous materials and a wide range of initial conditions.

1. Introduction

If a detailed analysis of the flow field that develops inside a porous medium which is struck head-on by a shock wave is required, then the process should be analysed using the multi-phase approach. In this approach, the porous medium is considered as multi-phase in which the various phases interact with each other. A detailed description of this approach was given by Baer & Nunziato (1986). A one-dimensional two-phase analysis of air as the fluid phase was presented by Baer (1988) and Powers, Stewart & Krier (1989). In addition to numerical solutions, Baer (1988) and Powers *et al.* (1989) also presented simplified analytical models for calculating the jump conditions across compaction waves in rigid porous materials.

Biot (1956) was probably the first to apply the notion of wave propagation to porous media. This was basically in terms of microscopic representations of the phase balance equations with the framework of the theory of mixtures. A large number of papers have appeared in the literature following Biot's pioneering work. Among the recent ones are those by Smeulders, de la Rosette & van Dongen (1992), Degrande & de Roeck (1992) and Nigmatulin & Gubaidullin (1992). Most refer to the linear acoustic waves which occur when the momentum dissipation terms dominate. As an example, Attenborough (1982) presented a theory dealing with the motion of sound waves through an ideal saturated porous matrix with parallel cylindrical pores. Using microscopic physical parameters, he extended this to account for randomly distributed pores. An extensive literature survey of similar approaches is given by Corapcioglu (1991).

Macroscopic momentum and energy balance equations, for a saturated porous medium, were developed by Levy *et al.* (1995) by conducting a dimensional analysis of the macroscopic balance equations of Bear *et al.* (1992) and Sorek *et al.* (1992). The

model developed is different to those mentioned above in its approach and hence yields different terms in the governing equations. It is novel in establishing the macroscopic theoretical basis for nonlinear wave motion in multi-phase deformable porous media. The model is based on conceptualizing the porous medium as a continuum composed of interacting compressible solid and fluid phases (saturated porous media). Macroscopic physical laws expressing mass, momentum and energy balances for the fluid and the solid matrix are formulated on the basis of the representative elementary volume (REV) concepts presented by Bear & Bachmat (1990). These macroscopic balance equations are composed of averaged flux terms together with integrals of microscopic exchange flux terms at the solid–fluid interface. Some unique macroscopic parameters which arise from the averaging process are the tortuosity factor which represents a tensor associated with the matrix directional cosines, the hydraulic radius of the pore spaces and the porosity which represents the volume fraction of the pores filled by the fluid. Note that unlike models developed in the past (e.g. Baer 1988), which account only for the properties of the phases, the macroscopic model developed in the course of this study also accounts for geometrical properties. Hence, in addition, the speed of the wave is also a function of the porous material structure. Unlike Bear & Bachmat (1990), Levy et al. (1995) showed that a Forchheimer term should be included as an additional macroscopic inertial term at the solid–fluid interface.

A dimensional analysis was applied to the macroscopic balance equations of the phases after the simultaneous onset of abrupt changes of the pressure and temperature of the fluid. Levy et al. (1995) obtained four significant evolution periods. In the first evolution period, pressure, temperature and stress are spatially distributed without attenuation. The vertical stress, however, is linearly dependent on gravity. In the second evolution period, they noted the rise of nonlinear wave forms. In the third evolution period, the inertial and dissipation terms were found to be of the same order and, consequently, the entire macroscopic Navier–Stokes equations should be considered. In the fourth evolution period, the inertial terms were found to be negligible in comparison to the dissipation terms. Assuming that the friction between the solid and the fluid is higher than that between the fluid layers, the nonlinear Darcy law (i.e. including a Forchheimer term) for the momentum balance equation of the fluid is obtained. Since the set of equations obtained was too complex to be solved analytically, subsequent investigations were aimed at simplifying the full set of governing equations by introducing simplifying assumptions, and then solving analytically the simplified models.

Based on the findings of Powers et al. (1989) the governing equations were simplified by Levy et al. (1993b) who proposed analytical expressions for calculating the jump conditions of the solid-phase properties across compaction waves in rigid porous materials. These expressions were found by solving the solid-phase balance equations without the interacting terms with the gaseous phase. This was justified by neglecting the gaseous-phase terms in the non-dimensional form of the overall conservation equations. The predictions of the model developed by Levy et al. (1993b) were found to be better than those proposed by Powers et al. (1989) when they were compared to the experimental results of Sandusky & Liddiard (1985).

In Bear & Sorek (1990) a mathematical model of an abrupt pressure impact applied to a compressible fluid flowing through saturated porous materials under isothermal conditions was developed. It was shown that during a certain time period, following the onset of the pressure change, the macroscopic fluid momentum balance equation conforms to a wave form. Krylov et al. (1996) presented a one-dimensional simple analytical solution of this wave equation. The wave equation was transformed to

Euler's equation describing the motion of a 'new' fluid with properties related to the fluid which actually occupies the pores of the porous material. A similar analytical solution was presented by Sorek *et al.* (1996) for the non-isothermal case; they presented a method leading to generalized forms for fluid density, pressure and temperature. Using these generalized properties they wrote Euler's equation as the one-dimensional expression for the analytical solution of the fluid equation of motion. To obtain this, the porosity, the matrix strain and temperature of the solid were developed as explicit function of the pressure.

In a subsequent study, Levy *et al.* (1996) developed a macroscopic one-dimensional analytical model for describing wave propagation in rigid porous media. Unlike Krylov *et al.* (1996) and Sorek *et al.* (1996), who neglected the momentum and energy exchanges between the two phases and assumed that the coupling between them was only due to the effective stress, in this study the momentum and energy exchanges between the two phases was also accounted for. Based on the dimensional analysis of Levy *et al.* (1995), who showed that the linear Darcy term was much smaller than the nonlinear Forchheimer term, only the Forchheimer term appeared in the momentum and energy exchanges between the two phases. In addition, it was assumed in this model that both the porosity and the temperature of the solid phase remain constant and that the inertial force of the solid phase is negligibly small.

Now that various simplified sets of the governing equations have been solved analytically, the aim of the present study is to solve the full one-dimensional set as developed and presented by Levy *et al.* (1995). Owing to its complexity an analytical solution is out of the question. This naturally leaves only one possibility, namely a numerical solution. It should be noted here that to the best of the authors' knowledge such a solution has not been conducted as yet. Neither have the compaction waves been simulated in a porous medium described below, a TVD-based computer code for solving the governing equations was developed. Its predictions were compared to experimental results and very good to excellent agreement was evident. Many more details can be found in Levy (1995).

2. Three-dimensional governing equations

A detailed derivation of the three-dimensional macroscopic governing equations describing the flow field in porous media was presented by Levy *et al.* (1995). In the following only the assumptions used in the derivation of the governing equations and the final form of the equations are given. The porous material is assumed to be 'rigid' in the loose relative sense commonly applied to porous materials in general and foams in particular, i.e. that deformations do not exceed a few percent.

2.1. *The assumptions*

The following assumptions are used. The fluid is ideal (i.e. $\mu_f = 0$ and $\lambda_f = 0$ where μ_f is the dynamic viscosity and λ_f is the thermal conductivity). The fluid is a perfect gas. The dispersive and diffusive mass fluxes of the fluid, and the dispersive flux of the solid, are much smaller than the corresponding advective ones and may, therefore, be neglected. The dispersive flux of momentum is much smaller than the advective flux and may, therefore, be neglected. The microscopic solid–fluid interfaces are material surfaces with respect to the mass of both phases. The solid matrix is thermoelastic, and is assumed to undergo small deformations only. The stress–strain relationship for the solid, at the microscopic level, and for the solid matrix, at the macroscopic level, have the same form. The material of which the skeleton of the porous medium is made is

incompressible. The specific heats at constant volume, C_f, and that at constant strain, C_s, for the solid, are constant. The energy processes for the fluid and for the solid are reversible. There are no external energy sources. The energy associated with viscous dissipation is negligibly small. The conductive and dispersive heat fluxes of the phases are negligibly small when compared to their advective heat flux. The rate of heat transferred between the fluid and solid phases is negligibly small.

2.2. *The balance equations*

The macroscopic mass balance equation for the fluid phase is

$$\frac{\partial \phi \rho_f}{\partial t} = -\nabla \cdot \phi \rho_f V_f, \tag{1}$$

where ρ_f is the density of the fluid, V_f denotes its velocity vector and ϕ denotes porosity.

The macroscopic mass balance equation for the solid phase is

$$\frac{\partial (1-\phi)\rho_s}{\partial t} = -\nabla \cdot (1-\phi)\rho_s V_s, \tag{2}$$

where ρ_s is the density of the solid (assumed to be constant) and V_s denotes its velocity vector.

The macroscopic momentum balance equation for the fluid phase is

$$\frac{\partial \phi \rho_f V_f}{\partial t} = -\nabla \cdot \phi \rho_f V_f V_f - \phi T^* \nabla P - \phi \rho_f g T^* \nabla Z - \frac{c_f}{2\Delta_f^2} \tilde{F} \phi \rho_f (V_f - V_s)(V_f - V_s), \tag{3}$$

where P, which denotes the pressure of the fluid, is prescribed by the equation of state (see equation (7)), g denotes the acceleration due to gravity in the Z-direction, $\tilde{F}$ and T^* denote the Forchheimer tensor for an isotropic solid matrix and the tortuosity tensor associated with the directional cosines at the solid–fluid interface, respectively, c_f denotes a shape factor, and Δ_f denotes the hydraulic radius of the pore spaces.

The macroscopic momentum balance equation for the solid phase is

$$\frac{\partial (1-\phi)\rho_s V_s}{\partial t} = -\nabla \cdot [(1-\phi)\rho_s V_s V_s] - (1-\phi) T_s^* \nabla P$$

$$+ \nabla \sigma_s' + (1-\phi)\rho_s g \nabla Z + \frac{c_f}{2\Delta_f^2} \tilde{F} \phi \rho_f (V_f - V_s)(V_f - V_s), \tag{4}$$

where σ_s' denotes the macroscopic constitutive relation for the effective stress of a thermoelastic solid matrix as given Bear *et al.* (1992), see equation (8).

The macroscopic energy balance equation for the fluid phase is

$$\frac{\partial}{\partial t}[\phi \rho_f (C_f T_f + \tfrac{1}{2} V_f^2)] = -\nabla \cdot [\phi \rho_f V_f (C_f T_f + \tfrac{1}{2} V_f^2)]$$

$$- T^* \nabla \phi P V_f + T^* P V_s \nabla \phi - \frac{c_f}{2\Delta_f^2} \tilde{F} \phi \rho_f (V_f - V_s)(V_f - V_s) V_s, \tag{5}$$

where T_f and C_f are the temperature and the specific heat at constant volume of the fluid phase, respectively.

The macroscopic energy balance equation for the solid phase is

$$\frac{\partial}{\partial t}[(1-\phi)\,\rho_s(C_s\,T_s + \tfrac{1}{2}V_s^2)] = -\nabla\cdot[(1-\phi)\,\rho_s\,V_f(C_s\,T_s + \tfrac{1}{2}V_s^2)]$$

$$+\nabla\sigma_s'\,V_s - T^*\nabla(1-\phi)\,PV_s - T^*PV_s\,\nabla\phi + \frac{c_f}{2\varDelta_f^2}\tilde{F}\phi\rho_f(V_f-V_s)(V_f-V_s)\,V_s, \quad (6)$$

where T_s and C_s are the temperature and the specific heat at constant strain of the solid phase, respectively.

The equation of state for the fluid phase (i.e. a perfect gas) is

$$P = \rho_f\,\Re T_f; \tag{7}$$

here $\Re$ is the specific gas constant.

The effective stress for a thermoelastic solid matrix, which undergoes small deformations only, is

$$\sigma_s' = \lambda_s''\,\epsilon_{skel}\,I + \mu_s'\,\varepsilon_{skel} - \eta(T_s - T_{s_0})\,I, \tag{8}$$

where μ_s', λ_s'' and η denote Lame constants of a thermoelastic solid and I denotes a unit tensor. The macroscopic strain tensor for the solid matrix, ε_{skel}, is defined for small deformations by the compatibility law

$$\varepsilon_{skel} = \tfrac{1}{2}[\nabla w_s + (\nabla w_s)^T], \tag{9}$$

in which w_s denotes the displacement vector of the solid matrix. The volumetric strain ($\equiv$ dilatation), ϵ_{skel}, is given by

$$\epsilon_{skel} = \nabla\cdot w_s. \tag{10}$$

Combining (10) and (2) while recalling that $\rho_s =$ constant (i.e. the solid material of which the porous matrix is made is incompressible) results in

$$\nabla\cdot V_s = \frac{1}{1-\phi}\frac{D_s\,\phi}{Dt} = \frac{D_s\,\epsilon_{skel}}{Dt}, \quad \frac{D_s(\ )}{Dt} \equiv \frac{\partial}{\partial t}(\ ) + V_s\cdot\nabla(\ ), \tag{11}$$

in which the following definition has been used:

$$V_s \equiv \frac{D_s\,w_s}{Dt}. \tag{12}$$

2.3. One-dimensional governing equations

In the present study, the one-dimensional version of the above three-dimensional form of the governing equations were solved. In a vector form these equations are written as follows:

$$\frac{\partial U}{\partial t} + \frac{\partial F}{\partial x} = Q. \tag{13}$$

The variables vector, U, is defined by

$$U = [r_f, r_s, m_f, m_s, E_f, E_s]^T, \tag{14}$$

where

$$\left.\begin{array}{llll} r_f \equiv \phi\rho_f, & m_f \equiv r_f\,V_f, & r_s \equiv (1-\phi)\rho_s, & m_s \equiv r_s\,V_s, \\ E_f \equiv r_f\,e_f = r_f(C_f\,T_f + \tfrac{1}{2}V_f^2), & E_s \equiv r_s\,e_s = r_s(C_s\,T_s + \tfrac{1}{2}V_s^2). \end{array}\right\} \tag{15}$$

The flux vector, F, is

$$
F = \begin{bmatrix}
m_f \\
m_s \\
\dfrac{m_f^2}{r_f} + T^* \phi P \\
\dfrac{m_s^2}{r_s} - \sigma_s' + (1 - \phi T^*) P \\
\dfrac{m_f}{r_f} (E_f + T^* \phi P) \\
\dfrac{m_s}{r_s} (E_s - \sigma_s' + (1 - \phi T^*) P)
\end{bmatrix}.
\tag{16}
$$

The source vector, Q, is

$$
Q = \begin{bmatrix}
0 \\
0 \\
T^* P \dfrac{\partial \phi}{\partial x} - \tilde{F} r_f \left| \dfrac{m_f}{r_f} - \dfrac{m_s}{r_s} \right| \left(\dfrac{m_f}{r_f} - \dfrac{m_s}{r_s} \right) \\
- T^* P \dfrac{\partial \phi}{\partial x} + \tilde{F} r_f \left| \dfrac{m_f}{r_f} - \dfrac{m_s}{r_s} \right| \left(\dfrac{m_f}{r_f} - \dfrac{m_s}{r_s} \right) \\
\dfrac{m_s}{r_s} \left(T^* P \dfrac{\partial \phi}{\partial x} - \tilde{F} r_f \left| \dfrac{m_f}{r_f} - \dfrac{m_s}{r_s} \right| \left(\dfrac{m_f}{r_f} - \dfrac{m_s}{r_s} \right) \right) \\
\dfrac{m_s}{r_s} \left(- T^* P \dfrac{\partial \phi}{\partial x} + \tilde{F} r_f \left| \dfrac{m_f}{r_f} - \dfrac{m_s}{r_s} \right| \left(\dfrac{m_f}{r_f} - \dfrac{m_s}{r_s} \right) \right)
\end{bmatrix},
\tag{17}
$$

where ϕP and σ_s' which appear in (16) are defined as follows:

$$
\phi P = (\gamma - 1) [E_f - m_f^2 / 2 r_f],
\tag{18}
$$

$$
\sigma_s' = E_\epsilon \epsilon - E_T C_s (T_s - T_{s0}).
\tag{19}
$$

In the above equations $E_\epsilon (\equiv \lambda_s'' + \mu_s')$ and $E_T (\equiv \eta / C_s)$ are the one-dimensional macroscopic Lame coefficients for a thermoelastic solid. With the aid of definitions (15) the porosity can be written as

$$
\phi = 1 - r_s / \rho_s.
\tag{20}
$$

By solving equation (2) analytically and with the aid of (15), the strain can be expressed as a function of the porosity as

$$
\epsilon = 1 - r_s / r_{s_0}.
\tag{21}
$$

With the aid of (15), equation (19) can be rewritten as

$$
\sigma_s' = E_\epsilon \left(\frac{r_{s0} - r_s}{r_{s0}} \right) - E_T \left(\frac{E_s}{r_s} - \frac{E_{s0}}{r_{s0}} - \frac{m_s^2}{2 r_s^2} + \frac{m_{s0}^2}{2 r_{s0}^2} \right).
\tag{22}
$$

The above set of equations consists of six differential equations, described by equations (13) and (14), and six unknowns namely: r_f, r_s, m_f, m_s, E_f and E_s. Consequently, in principle, the equations are complete and can be solved. However, owing to the complexity of the equations, an analytical solution of the set is impossible. Note that simplified cases were solved analytically by Levy *et al.* (1993*b*, 1996), Krylov *et al.* (1996) and Sorek *et al.* (1996). Some of these solutions were verified by comparison with experimental results. Instead, a numerical solution has been

performed in the present study. Details of the numerical method are given in the next section.

Note that in writing equation (13) we assumed that the gradients of the porosity were very small and therefore they might be written as source terms in the source vector, Q, given by (17). As a result Q contains derivative terms and thus affects the character of the equations (hyperbolic rather than elliptic-hyperbolic). This is very convenient for numerical purposes and is correct only when the gradients of the porosity are very small as is the case in this study. Applying this procedure removes the ill-posedness associated with the elliptic-hyperbolic character of the equations which is usually manifested in highly oscillatory solutions as the mesh is refined.

3. The numerical method

An upwind TVD shock-capturing scheme, originally developed by Harten (1983), was extended to solve the problem of two-phase flow which described wave propagation and interaction in saturated porous media. The scheme for solving equation (13) can be written in the following conservative form:

$$U_j^{n+1} = U_j^n - \lambda(\bar{F}_{j+1/2} - \bar{F}_{j-1/2}) + \Delta t Q_j, \tag{23}$$

where the parameter λ is defined by

$$\lambda \equiv \Delta t / \Delta x \tag{24}$$

and the numerical flux, $\bar{F}_{j+1/2}$, is evaluated from

$$\bar{F}_{j+1/2} = \frac{1}{2}\left[F(U_j^n) + F(U_{j+1}^n) - \frac{1}{\lambda}\sum_{k=1}^{6}\beta_{j+1/2}^k R_{j+1/2}^k\right], \tag{25}$$

$$\beta_{j+1/2}^k = \Psi^k(\nu_{j+1/2}^k + \gamma_{j+1/2}^k)\alpha_{j+1/2}^k - (g_j^k + g_{j+1}^k), \tag{26}$$

$$\nu_{j+1/2}^k = \lambda a^k(U_{j+1/2}), \tag{27}$$

$$\gamma_{j+1/2}^k = \begin{cases} (g_{i+1}^k - g_i^k)/\alpha_{j+1/2}^k, & \alpha_{j+1/2}^k \neq 0 \\ 0, & \alpha_{j+1/2}^k = 0, \end{cases} \tag{28}$$

$$g_i^k = \text{sgn}(\tilde{g}_{j+1/2}^k)\max[0, \min(|\tilde{g}_{j+1/2}^k|, \tilde{g}_{j-1/2}^k \text{sgn}(\tilde{g}_{j+1/2}^k))], \tag{29}$$

$$\tilde{g}_{j+1/2}^k = \tfrac{1}{2}[\Psi^k(\nu_{j+1/2}^k) - (\nu_{j+1/2}^k)^2]\alpha_{j+1/2}^k, \tag{30}$$

$$\Psi(x) = \begin{cases} x^2/4\xi + \xi, & |x| < 2\xi \\ |x|, & |x| \geqslant 2\xi, \end{cases} \tag{31}$$

$$\xi = \begin{cases} 0.1, & (\partial a^k/\partial U)R^k \neq 0 \\ 0, & (\partial a^k/\partial U)R^k = 0. \end{cases}$$

The eigenvalues, a^k, of the Jacobian matrix $A(U) = \partial F/\partial U$ were found symbolically by using the application *Mathematica* to be

$$a^1 = V_s - a_s, \quad a^2 = V_f - a_f, \quad a^3 = V_s, \quad a^4 = V_f, \quad a^5 = V_f + a_f, \quad a^6 = V_s + a_s, \tag{32}$$

where a_f and a_s are the equivalent speeds of sound of the fluid and the solid phases, respectively. They can be expressed as

$$a_f^2 = \frac{\phi P(1 - T^* + \gamma T^*)T^*}{r_f}, \tag{33}$$

and

$$a_s^2 = \frac{E_\epsilon}{r_{s0}} + \left(\frac{\rho_s}{(\rho_s - r_s)} + \frac{E_T(\rho_s(1 - T^*) + T^* r_s)}{r_s^2} \right) \frac{\phi P}{(\rho_s - r_s)} - \frac{E_T E_\epsilon}{r_s^2} \left(\frac{r_{s0} - r_s}{r_{s0}} \right)$$
$$+ \frac{E_T^2}{r_s^2} \left(\frac{E_s}{r_s} - \frac{E_{s0}}{r_{s0}} - \frac{m_s^2}{2r_s^2} + \frac{m_{s0}^2}{2r_{s0}^2} \right). \quad (34)$$

The corresponding right eigenvectors, R^k, were found to be

$$R^1 = \begin{bmatrix} 0 \\ 1 \\ 0 \\ V_s - 1_s \\ 0 \\ H_s - V_s a_s \end{bmatrix}, \quad R^2 = \begin{bmatrix} 1 \\ -\dfrac{a_f^2(\rho_s - (\rho_s - r_s) T^*)}{(a_s^2 - \vartheta_1^2)(\rho_s - r_s) T^*} \\ V_f - a_f \\ \dfrac{a_f^2(\rho_s - (\rho_s - r_s) T^*)(\vartheta_1 - V_s)}{(a_s^2 - \vartheta_1^2)(\rho_s - r_s) T^*} \\ H_f - V_f a_f \\ \dfrac{a_f^2(\rho_s - (\rho_s - r_s) T^*)(\vartheta_1 V_s - H_s)}{(a_s^2 - \vartheta_1^2)(\rho_s - r_s) T^*} \end{bmatrix}, \quad R^3 = \begin{bmatrix} 0 \\ 1 \\ 0 \\ V_s \\ 0 \\ H_s - \dfrac{r_s a_s^2}{E_T} \end{bmatrix}$$

$$(35\,a\!-\!c)$$

$$R^4 = \begin{bmatrix} 1 \\ 0 \\ V_f \\ 0 \\ V_f^2 \\ 0 \end{bmatrix}, \quad R^5 = \begin{bmatrix} 1 \\ -\dfrac{a_f^2(\rho_s - (\rho_s - r_s) T^*)}{(a_s^2 - \vartheta_2^2)(\rho_s - r_s) T^*} \\ V_f + a_f \\ -\dfrac{a_f^2(\rho_s - (\rho_s - r_s) T^*)(\vartheta_2 + V_s)}{(a_s^2 - \vartheta_2^2)(\rho_s - r_s) T^*} \\ H_f + V_f a_f \\ -\dfrac{a_f^2(\rho_s - (\rho_s - r_s) T^*)(\vartheta_2 V_s + H_s)}{(a_s^2 - \vartheta_2^2)(\rho_s - r_s) T^*} \end{bmatrix}, \quad R^6 = \begin{bmatrix} 0 \\ 1 \\ 0 \\ V_s + a_s \\ 0 \\ H_s + V_s a_s \end{bmatrix},$$

$$(35\,d\!-\!f)$$

where

$$H_f = \frac{E_f + T_f^* \phi P}{r_f} \quad (36)$$

and

$$H_s = \frac{E_s}{r_s} - E_\epsilon \left(\frac{r_{s0} - r_s}{r_s r_{s0}} \right) + \frac{E_T}{r_s} \left(\frac{E_s}{r_s} - \frac{E_{s0}}{r_{s0}} - \frac{m_s^2}{2r_s^2} + \frac{m_{s0}^2}{2r_{s0}^2} \right) + \frac{(1 - \phi T^*) P}{r_s} \quad (37)$$

are the enthalpies of the fluid and the solid phases, respectively. ϑ_1 and ϑ_2 are defined by

$$\vartheta_1 = a_f - V_f + V_s, \quad \vartheta_2 = a_f + V_f - V_s \quad (38)$$

The parameters $\alpha_{j+1/2}^k$ were found by solving the linear equations

$$U_{j+1} - U_j = \sum_{k=1}^6 \alpha_{j+1/2}^k R_{j+1/2}^k \quad (39)$$

to be

$$\begin{aligned} \alpha_{j+1/2}^1 &= \frac{(C_3 - C_4)}{2} + \frac{(\rho_s - (\rho_s - \hat{r}_s) T^*) \, \hat{a}_f^2((\hat{a}_s + \hat{V}_f - \hat{V}_s) C_1 - \hat{a}_f C_2)}{2(\rho_s - \hat{r}_s) T^* \hat{a}_s(\hat{a}_s - \hat{\vartheta}_1)(\hat{a}_s + \hat{\vartheta}_2)}, \\[2mm] \alpha_{j+1/2}^2 &= (C_1 - C_2)/2, \quad \alpha_{j+1/2}^3 = [r_s] - C_3, \\[2mm] \alpha_{j+1/2}^4 &= [r_f] - C_1, \quad \alpha_{j+1/2}^5 = (C_1 + C_2)/2, \\[2mm] \alpha_{j+1/2}^6 &= \frac{(C_3 + C_4)}{2} + \frac{(\rho_s - (\rho_s - \hat{r}_s) T^*) \, \hat{a}_f^2((\hat{a}_s - \hat{V}_f + \hat{V}_s) C_1 + \hat{a}_f C_2)}{2(\rho_s - \hat{r}_s) T^* \hat{a}_s(\hat{a}_s + \hat{\vartheta}_1)(\hat{a}_s - \hat{\vartheta}_2)}, \end{aligned} \right\} \quad (40)$$
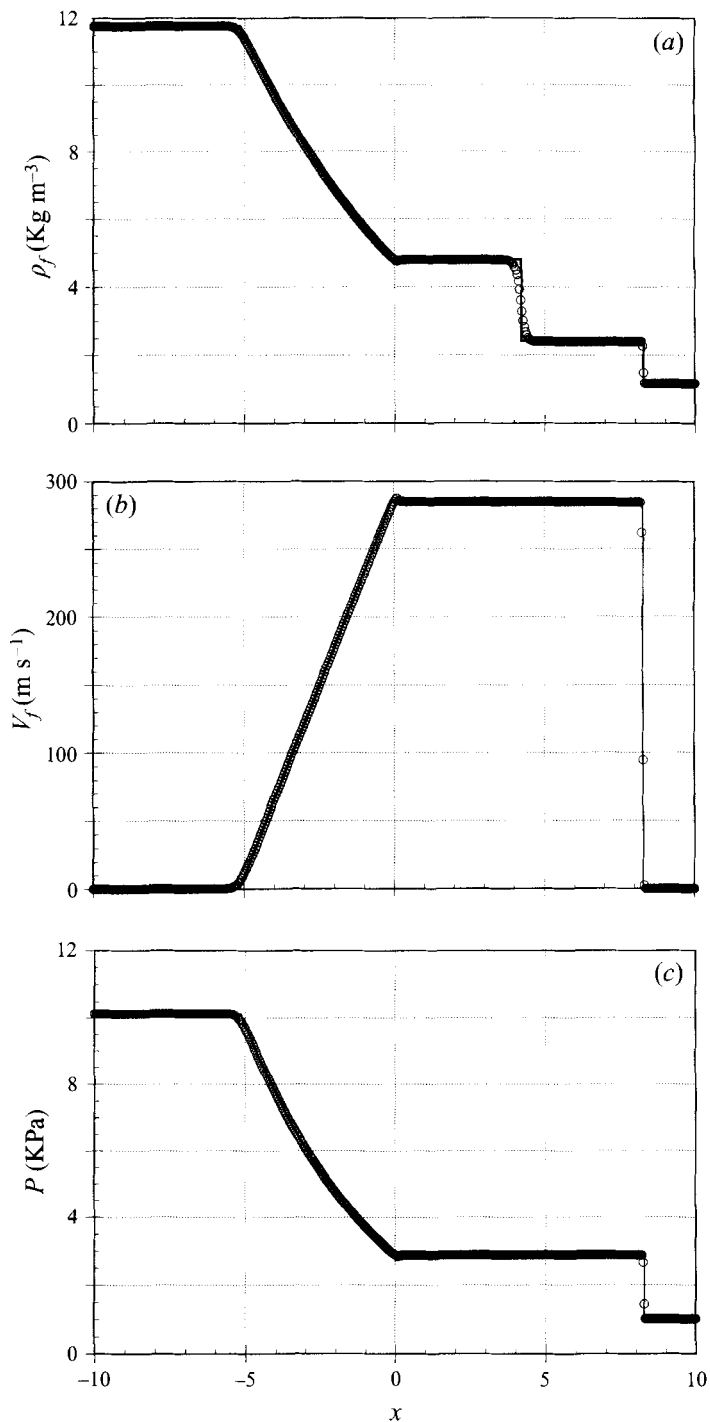
FIGURE 1. Comparison between the analytical solutions (solid lines) and the numerical predictions (open circles) of the classical one-dimensional shock tube problem: (a) density, (b) velocity and (c) pressure.

where $[b] \equiv b_{i+1} - b_i$, $\hat{b}$ is an average property in the interval $[x_{i+1} - x_i]$ and the parameters C_k (for $k = 1, 2, 3, 4$) are as follows:

$$C_1 = \frac{(\gamma - 1)\, T^* ([E_f] + \frac{1}{2}\hat{V}_f^2[r_f] - \hat{V}_f[m_f])}{\hat{a}_f^2}, \qquad C_2 = \frac{[m_f] - \hat{V}_f[r_f]}{\hat{a}_f},$$

$$C_3 = \frac{E_T\left([E_s] + \left(\hat{V}_s^2 - \hat{H}_s + \frac{\hat{r}_s \hat{a}_s^2}{E_T}\right)[r_s] - \hat{V}_s[m_s]\right)}{\hat{r}_s \hat{a}_s^2}, \qquad C_4 = \frac{[m_s] - \hat{V}_s[r_s]}{\hat{a}_s}. \tag{41}$$

The boundary condition on the shock-tube endwall was simulated by using the image point method. The computational grid system was composed of 500 nodes. The computations were performed with a DecStation 5000/260 and an Indy R4400/150.

The performance of the TVD scheme developed here was checked by simulating the well-known one-dimensional shock-tube problem. Figure 1 illustrates the analytical solution (solid lines) and the numerical predictions (open circles) for the fluid density, velocity and pressure distributions. The initial conditions for this simulation were

$$U(x) = \begin{cases} U_L, & x \leqslant 0 \\ U_R, & x > 0, \end{cases}$$

where

$$U_L = \begin{bmatrix} r_f \\ r_s \\ m_f \\ m_s \\ E_f \\ E_s \end{bmatrix}_L = \begin{bmatrix} 11.7683 \\ 0 \\ 0 \\ 0 \\ 2\,533\,125 \\ 0 \end{bmatrix}, \quad U_R = \begin{bmatrix} r_f \\ r_s \\ m_f \\ m_s \\ E_f \\ E_s \end{bmatrix}_R = \begin{bmatrix} 1.17683 \\ 0 \\ 0 \\ 0 \\ 253\,312.5 \\ 0 \end{bmatrix}.$$

The comparison between the analytical solutions and the numerical predictions of the present simulation clearly indicates that the numerical code developed here reproduces the one-dimensional shock-tube problem excellently.

4. Experimental study

The head-on collision of a planar shock wave with a rigid porous material was investigated experimentally in order to validate the predictions of the physical model and the numerical code. The experiments were conducted in the 75 mm × 75 mm shock tube of the School of Mechanical Engineering of the University of Witwatersrand in Johannesburg, South Africa. The incident-shock-wave Mach number range was $1.2 \leqslant M_s \leqslant 1.7$; the initial pressures and temperatures throughout the experimental study were about 830 mbar and about 288 K, respectively.

The rigid porous materials were made of silicon carbide (SiC) and alumina (Al_2O_3). The SiC manufactured porous material had either 10 or 20 pores per inch and the Al_2O_3 manufactured porous material had either 30 or 40 pores per inch. The porosity of these porous materials as well as the initial length, L_0, of the samples which were cut from them are given in table 1. The porosity, ϕ, was simply calculated from $\phi = 1 - \rho_b/\rho_s$, where ρ_b is the bulk density of the porous material and ρ_s is the material density of the skeleton of which the porous material is made. Note that the above expression is limited to gas-saturated porous materials as was the case in the present study. The cross-section dimensions of the samples were identical to those of the shock-tube test section. Consequently, they could not expand sideways but only be
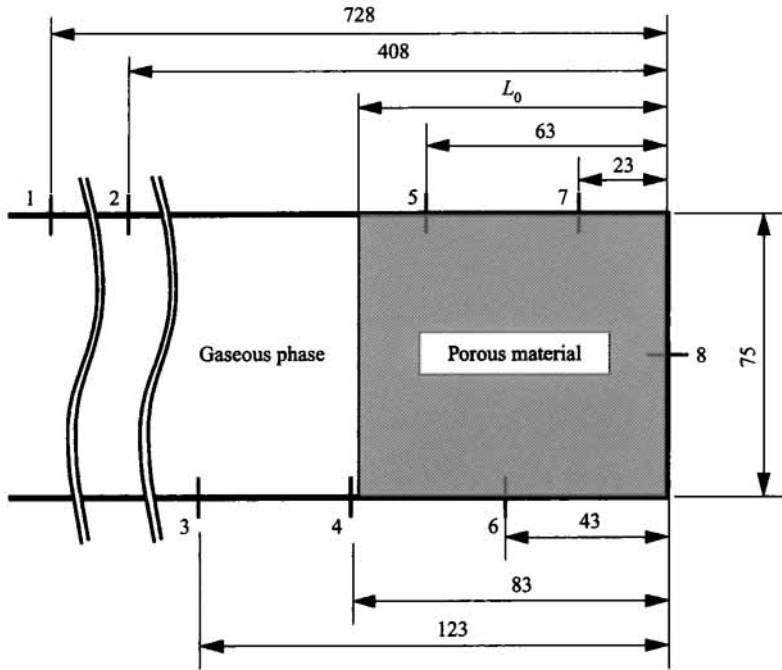
FIGURE 2. Schematic illustration of the experimental set-up and the locations of pressure transducers (numbered 1–8). All dimensions are in mm.

The sample material	Sample type	Pores per inch (p.p.i.)	Air porosity	Sample length (mm)	$\tilde{F}$ (m^{-1})	T^*
Silicon Carbide	I	10	0.728 ± 0.016	40, 60, 81	300	0.7
(SiC)	II	20	0.745 ± 0.001	41, 62, 83	500	0.7
Alumina	III	30	0.814 ± 0.010	48, 93	900	0.75
(Al$_2$O$_3$)	IV	40	0.821 ± 0.007	50, 99	1800	0.75

TABLE 1. The experimental samples, and their tortuosity and Forchheimer factors. The structure of the porous material was open cell.

compressed in the direction of the propagation of the shock wave. Hence, they experienced a uni-axial strain (also known as tri-axial stress) compression. Twelve experiments were conducted with each sample. The models were mounted at the end of the driven section of the shock tube in such a way that their back edges were supported by the shock-tube endwall.

A schematic illustration of the experimental set-up used during the present experimental study is shown in figure 2. Although there were eight pressure transducer ports, only seven of them were actually used in each experiment. The pressure transducers in ports 1 and 2 were used to measure the incident-shock-wave velocity. Pressure transducers were mounted in ports 4, 5, 6, 7 and 8 for the samples having an initial length up to (inclusive) 83 mm (see table 1). For the alumina sample with an initial length of 99 mm the pressure transducer of port 4 was moved to port 3. This was done in order to have a measurement of the pressure changes caused by the shock wave which reflected backwards from the front edge of the porous material. The pressure data acquisition was every 4 μs (for more details see Levy *et al.* 1993*a*).

Sample material	Test number	Sample length (mm)	Initial pressure (KPa)	Initial temperature (K)	Shock Mach number, M_s
SiC 10 p.p.i.	1	40	83.04	290.0	1.378
	2	60	83.11	290.5	1.385
	3	81	83.41	290.5	1.377
	4	81	83.71	289.5	1.543
	5	81	83.70	290.5	1.734
SiC 20 p.p.i.	6	41	83.50	289.0	1.381
	7	41	83.44	289.5	1.533
	8	41	83.70	289.5	1.711
	9	62	83.62	290.0	1.378
	10	83	83.14	289.5	1.379
Al_2O_3 30 p.p.i.	11	48	82.84	292.0	1.374
	12	93	83.41	290.5	1.377
	13	93	83.36	291.0	1.539
	14	93	83.12	291.5	1.744
Al_2O_3 40 p.p.i.	15	50	83.09	292.0	1.374
	16	50	83.08	292.5	1.545
	17	50	83.10	292.5	1.741
	18	99	83.16	290.5	1.377

TABLE 2. The initial conditions for the various experiments.

5. Comparison between the numerical prediction and the experimental results, and discussion

In order to solve equation (13) and compare it to the experimental results, the various parameters, namely the macroscopic Lame coefficients for a thermoelastic solid E_ϵ and E_T, the Forchheimer factor $\tilde{F}$, the tortuosity T^*, and the intrinsic density of the solid matrix ρ_s, which appear in the physical model had to be estimated for each sample. Based on the properties of the materials of which the samples were made and the fact that the upper limit of the elastic stress reduces when the porosity increases, in a $(1-\phi)^2$ manner (see Gibson & Ashby 1988), the order of magnitudes of the macroscopic Lame coefficients, E_ϵ and E_T, were estimated to be identical for all the samples, at $E_\epsilon = 380 \times 10^7$ Pa and $E_T = 26.207$ Kg m^{-3}. The sensitivity of the predictions of the numerical code to these coefficients will be examined in a future study.

The intrinsic density of the solid matrix for all the samples (i.e. silicon carbide and alumina) as provided by the manufacturer (FOSECO South Africa Ltd) was $\rho_s = 2000 \pm 60$ Kg m^{-3}.

The tortuosity factors, T^*, for the various samples were found by estimating the ratio between the speed of sound of the air inside the porous medium, (33), and that in a pure air. The Forchheimer factors, $\tilde{F}$, for the various samples were found experimentally. In these experiments, each sample was mounted in a pipe and the pressure drop across it was measured as a function of the air flow rate. The pressure drop was found to be a parabolic function of the air velocity. This was done by assuming that the pressure drop depends linearly on the length of the sample. The values of the tortuosity and the Forchheimer factors, as obtained experimentally for the various samples, are also presented in table 1.

In order to validate the physical model and the numerical code, (13) was solved numerically for different samples and initial conditions and compared to experimental results. Table 2 represents the initial conditions of 18 different experiments. The
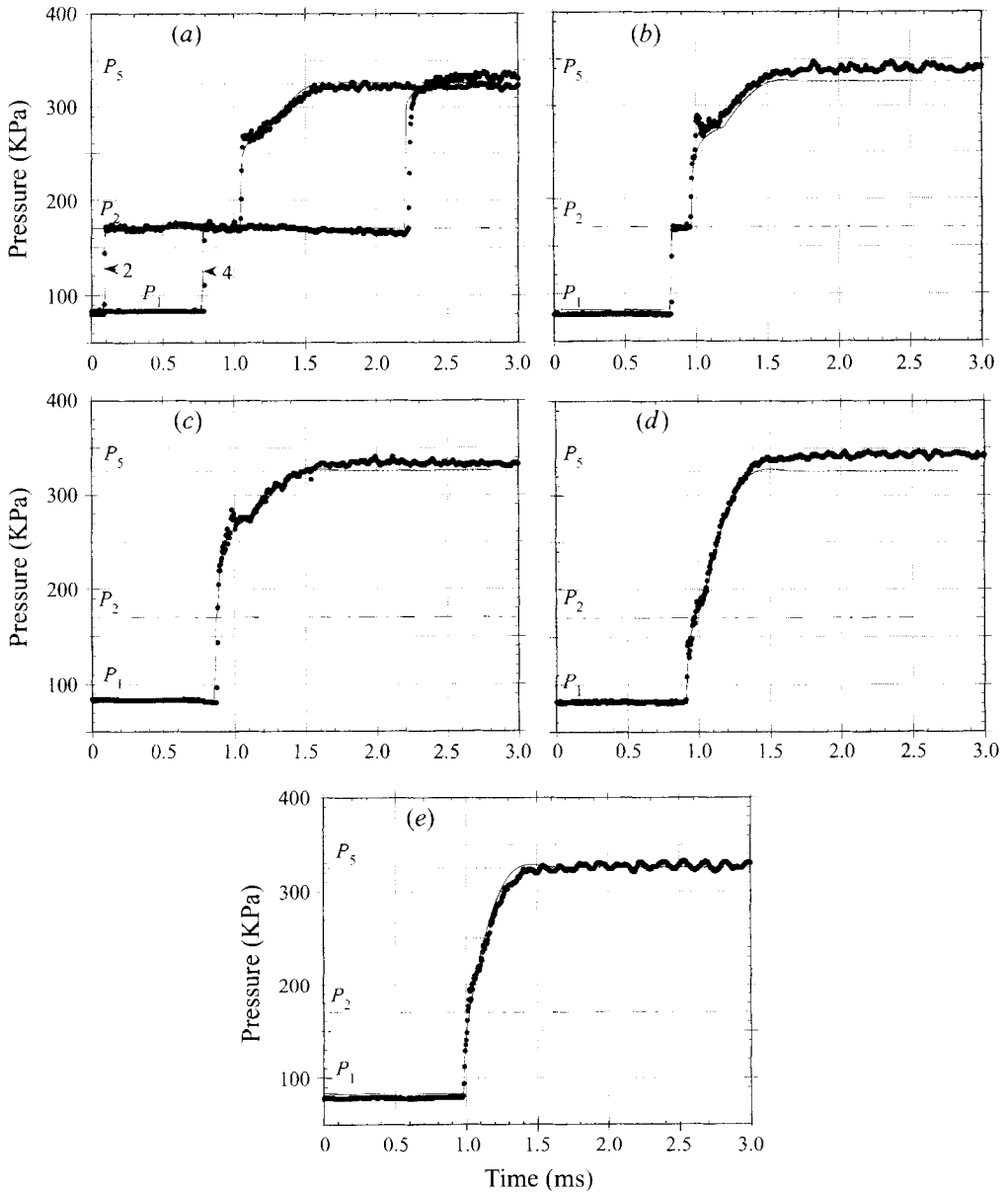
FIGURE 3. Typical results of the experimental results and their numerical simulations with a 40 mm long sample made of SiC having 10 pores per inch (i.e. sample 1 in table 1). The incident-shock-wave Mach number in this experiment was $M_s = 1.378$ (i.e. test number 1 in table 2). The pressure histories of the pure gas just ahead of the front edge of the porous material are shown in (a) and (b). The pressure histories of the gas occupying the pores of the porous material along the shock-tube sidewall and at its endwall are shown in (c), (d) and (e), respectively. The symbols represent the experimental results and the solid lines are the numerically predicted values. P_1 is the pressure ahead of both the incident and the transmitted shock waves, P_2 is the theoretical pressure which should have been reached behind the incident shock wave, and P_5 is the theoretical pressure which would have been reached had the incident shock wave reflected head-on from a solid endwall.
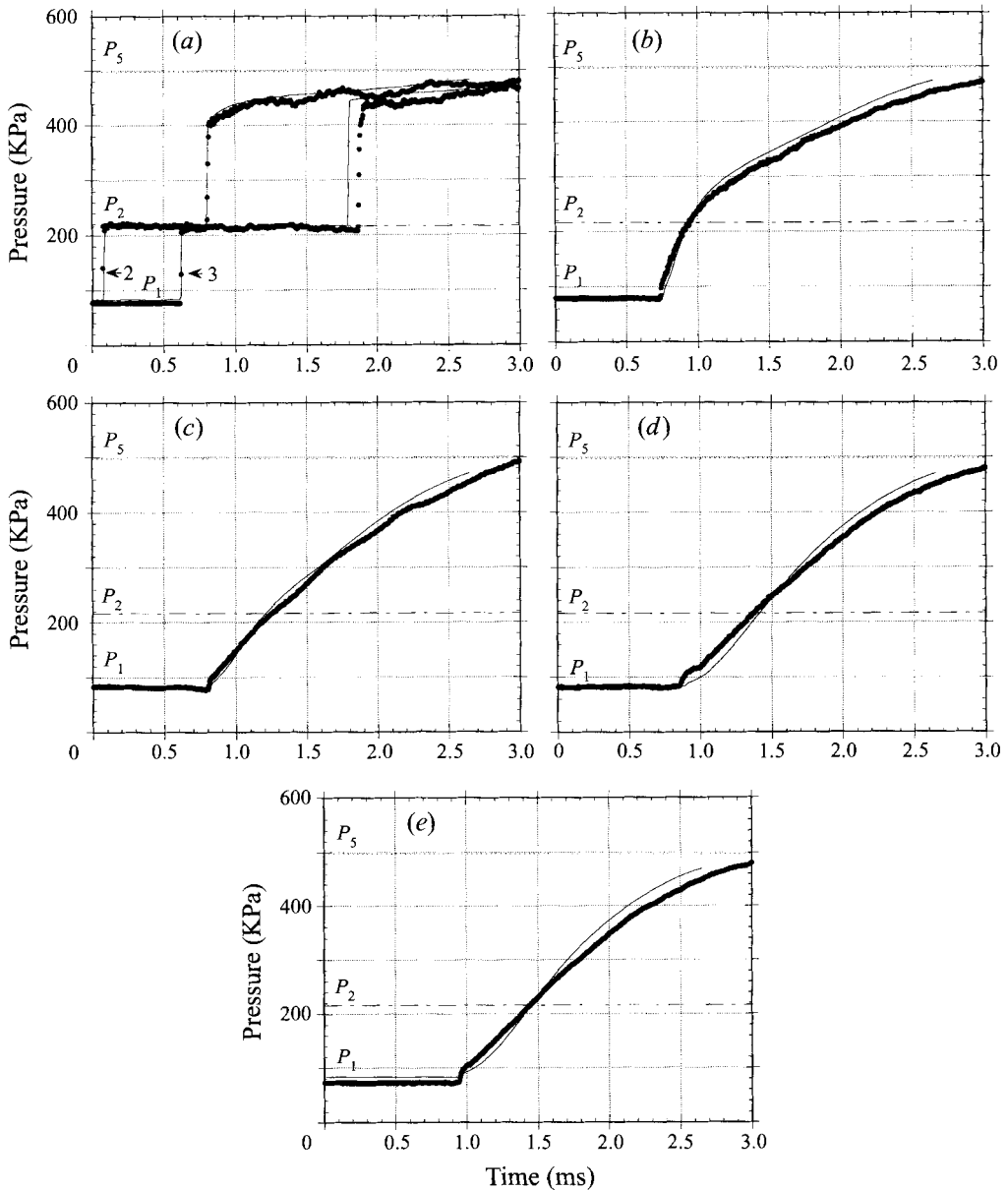
FIGURE 4. Typical results of the experimental results and their numerical simulations with a 40 mm long sample made of Al_2O_3 having 30 pores per inch (i.e. sample III in table 1). The incident-shock-wave Mach number in this experiment was $M_s = 1.539$ (i.e. test number 1 in table 2). The pressure histories of the pure gas just ahead of the front edge of the porous material are shown in (a). The pressure histories of the gas occupying the pores of the porous material along the shock-tube sidewall and at its endwall are shown in (b–e), respectively. The symbols represent the experimental results and the solid lines are the numerically predicted values. P_1, P_2, and P_5 are defined in the caption of figure 3.

comparison between the predictions of the numerical simulations and the experimental results, for the cases appearing in table 2, are given in Levy (1995).

Figures 3 (a–e) and 4 (a–e) represent typical experimental results and their numerical simulations for the SiC and Al_2O_3 samples, respectively. P_1 is the pressure ahead of

both the incident and the transmitted shock waves, P_2 is the theoretical pressure which should have been reached behind the incident shock wave, and P_5 is the theoretical pressure which should have been reached had the incident shock wave reflected head-on from a solid endwall. The symbols represent the experimental results and the solid lines are the numerically predicted values. The pressure histories of the pure gas just ahead of the front edge of the porous material are shown in figures 3(a, b) for the SiC and 4(a) for the Al_2O_3. The pressure histories of the gas occupying the pores of the porous material along the shock tube sidewall and at its endwall are shown in figures 3(c–e) for the SiC and 4(b–e) for the Al_2O_3.

Figure 3(a–e) illustrates the comparisons between the predictions of the numerical simulations and the pressure histories as recorded by the various pressure transducers for an experiment with a 40 mm long sample made of SiC having 10 pores per inch (i.e. sample I in table 1). The incident-shock-wave Mach number in this experiment was $M_s = 1.378$ (i.e. test number 1 in table 2). The pressure histories shown in figure 3(a–e) were recorded by the pressure transducers which were mounted in the ports numbered 2, 4, 5, 6, 7 and 8 in figure 2.

Figure 4(a–e) illustrates the comparisons between the predictions of the numerical simulations and the pressure histories as recorded by the various pressure transducers for an experiment with a 93 mm long sample made of Al_2O_3 having 30 pores per inch (i.e. sample III in table 1). The incident-shock-wave Mach number in this experiment was $M_s = 1.539$ (i.e. test number 13 in table 2). The pressure histories shown in figure 4(a–e) were recorded by the pressure transducers which were mounted in the ports numbered 2, 3, 5, 6, 7 and 8 in figure 2.

It is clearly evident from these comparisons that the agreement between the experimental and the numerical results is very good. Note that there are disagreements between the numerical and the experimental positions of the reflected shock wave after it had travelled to a relatively long distance from the front edges of the samples (see figures 3a and 4a). The agreement was better in the case of low incident-shock-wave Mach numbers and short samples. This may be caused by the way the porosity gradient terms were treated in the source vector, Q.

Although figures 3 and 4 describe the results of only two typical experiments, one in a silicon-carbide (SiC) sample and one in an alumina (Al_2O_3) sample, similar agreement was obtained in the comparisons with all the experiments which were conducted in the course of the present study. Details of all these comparisons are given in Levy (1995).

6. Conclusions

The general macroscopic balance equations, for a saturated rigid porous medium, were developed. Their one-dimensional versions were solved numerically using a TVD-based numerical code which was developed during the course of this study. The numerical predictions were compared to experimental results and good to excellent agreement was evident for different porous materials and for a wide range of initial conditions. To the best of the authors' knowledge, this is the first time that compaction waves have been successfully simulated inside a porous medium.

We would like to dedicate this study which is a part of Avi Levy's PhD research to Professor Ami Harten. It was decided in the early stages of this study to develop a TVD-based computer code for simulating the phenomenon. For this reason Professor Ami Harten was asked to act as an external examiner. Ami was quite skeptical about

the possibility of developing the code. As reported in this study a TVD-based code was finally developed and the agreement between its numerical predictions and the experimental results were found to be very good to excellent. Unfortunately, Ami did not live to see the results.

REFERENCES

ATTENBOROUGH, K. 1982 Acoustical characteristics of porous materials. *Phys. Rep.* **82**, 179–227.

BAER, M. R. 1988 Numerical studies of dynamic compaction of inert and energetic granular materials. *Trans. ASME J. Appl. Mech.* **55**, 36–43.

BAER, M. R. & NUNZIATO, J. W. 1986 A two-phase mixture theory for the deflagration to detonation transition (DDT) in reactive granular materials. *Intl J. Multiphase Flow* **12**, 861–889.

BEAR, J. & BACHMAT, Y. 1990 *Introduction to Modeling of Transport Phenomena in Porous Media*. Kluwer.

BEAR, J. & SOREK, S. 1990 Evolution of governing mass and momentum balances following an abrupt pressure impact in porous medium. *Transport in Porous Media* **5**, 169–185.

BEAR, J., SOREK, S., BEN-DOR, G. & MAZOR, G. 1992 Displacement waves in saturated thermoelastic porous media. I. Basic equations. *Fluid Dyn. Res.* **9**, 155–164.

BIOT, M. A. 1956 Theory of propagation of elastic waves in fluid-saturated porous solid. *J. Acoust. Soc. Am.* **28**, 168–191.

CORAPCIOGLU, M. Y. 1991 Wave propagation in porous media – a review. In *Transport Processes in Porous Media* (ed. J. Bear & M. Y. Corapcioglu), pp. 373–469. Kluwer.

DEGRANDE, G. & ROECK, G. DE 1992 FFT-based spectral analysis methodology for one-dimensional wave propagation in poroelastic media. *Transport in Porous Media* **9**, 85–97.

GIBSON, L. J. & ASHBY, M. F. 1988 *Cellular Solids – Structure & Properties*. Program Press, Hill Hall, Oxford.

HARTEN, A. 1983 High resolution schemes for hyperbolic conservation laws. *J. Comput. Phys.* **49**, 357–393.

KRYLOV, A., SOREK, S., LEVY, A. & BEN-DOR, G. 1996 Simple waves in saturated porous media. I. The isothermal case. *Japan Soc. Mech. Engrs Intl J.* **B39**, 294–298.

LEVY, A. 1995 Wave propagation in a saturated porous media. PhD thesis, Department of Mechanical Engineering, Ben-Gurion University of the Negev (in Hebrew).

LEVY, A., BEN-DOR, G., SKEWS, B. & SOREK, S. 1993*a* Head-on collision of normal shock waves with rigid porous materials. *Exps. Fluids* **15**, 183–190.

LEVY, A., BEN-DOR, G., SOREK, S. & BEAR, J. 1993*b* Jump conditions across strong compaction waves in gas saturated rigid porous media. *Shock Waves* **3**, 105–111.

LEVY, A., SOREK, S., BEN-DOR, G. & BEAR, J. 1995 Evolution of the balance equations in saturated thermoelastic porous media following abrupt simultaneous changes in pressure and temperature. *Transport in Porous Media* **21**, 241–268.

LEVY, A., SOREK, S., BEN-DOR, G. & SKEWS, B. 1996 Waves propagation in saturated rigid porous media: analytical model and comparison with experimental results. *Fluid Dyn. Res.* **17**, 49–65.

NIGMATULIN, R. I. & GUBAIDULLIN, A. A. 1992 Linear waves in saturated porous media. *Transport in Porous Media* **9**, 135–142.

OLIM, M., DONGEN, M. E. W. VAN, KITAMURA, T. & TAKAYAMA, K. 1994 Numerical simulation of the propagation of shock waves in compressible open-cell porous foams. *Intl J. Multiphase Flow* **20**, 557–568.

POWERS, J. M., STEWART, D. S. & KRIER, H. 1989 Analysis of steady compaction waves in porous materials. *Trans. ASME J. Appl. Mech.* **56**, 15–24.

SANDUSKY, H. W. & LIDDIARD, T. P. 1985 Dynamic compaction of porous beds. *NSWC TR* 83-256. NAVAL Surface Weapons Center, White Oak, MD, USA.

SKEWS, B. W. 1991 The reflected pressure field in the interaction of weak shock waves with a compressible porous foam. *Shock Waves* **1**, 205–211.

SKEWS, B. W., ATKINS, M. D. & SEITZ, M. W. 1993 The impact of shock wave on porous compressible foams. *J. Fluid Mech.* **253**, 245–265.

SMEULDERS, D. M. J., ROSETTE, S. P. M. DE LA & DONGEN, M. E. H. VAN 1992 Waves in partially saturated porous media. *Transport in Porous Media* **9**, 25–37.

SOREK, S., BEAR, J., BEN-DOR, G. & MAZOR, G. 1992 Shock waves in saturated thermoelastic porous media. *Transport in Porous Media* **9**, 3–13.

SOREK, S., KRYLOV, A., LEVY, A. & BEN-DOR, G. 1996 Simple waves in saturated porous media. II. The nonisothermal case. *Japan Soc. Mech. Engrs Intl J.* **B39**, 299–304.